INTERNATIONAL JOURNAL FOR NUMERICAL METHODS IN FLUIDS
Int. J. Numer. Meth. Fluids 2003; **43**:1355–1370 (DOI: 10.1002/fld.565)

Computation of strongly swirling confined flows with cubic eddy-viscosity turbulence models

Xiaodong Yang*,†,‡ and Huiyang Ma§,¶

Department of Physics, Graduate School of the Chinese Academy of Sciences, P.O. Box 3908, Beijing 100039, People's Republic of China

SUMMARY

An investigation on the predictive performance of four cubic eddy-viscosity turbulence models for two strongly swirling confined flows is presented. Comparisons of the prediction with the experiments show clearly the superiority of cubic models over the linear k–ε model. The linear k–ε model does not contain any mechanism to describe the stabilizing effects of swirling motion and as a consequence it performs poorly. Cubic models return a lower level of Reynolds stresses and the combined forced-free vortex profiles of tangential velocity close to the measurements in response to the interaction between swirl-induced curvature and stresses. However, a fully developed rotating pipe flow is too simple to contain enough flow physics, so the calibration of cubic terms is still a topic of investigation. It is shown that explicit algebraic stress models require fewer calibrations and contain more flow physics. Copyright © 2003 John Wiley & Sons, Ltd.

KEY WORDS: strongly swirling flow; confined flow; turbulence modelling; cubic eddy-viscosity models

1. INTRODUCTION

Swirling flows are widely used in industrial applications, such as combustion chambers and furnaces, to aid stabilizing the flame and create a region of strong shear to enhance mixing process. The structure of the turbulence is highly sensitive to the swirl-induced body forces. So the turbulence models used should contain an inherent mechanism capable of capturing this sensitivity. For a fully developed rotating pipe flow, the widely used standard k–ε model is well recognized to predict a solid body rotation for the tangential velocity while

* Correspondence to: Xiao-dong Yang, Department of Physics, Graduate School, Chinese Academy of Sciences, P.O. Box 3908, 100039 Beijing, People's Republic of China.
† E-mail: yangshield@yahoo.com.cn
‡ Graduate Student.
§ Professor.
¶ E-mail: hyma@163bj.com

Contract/grant sponsor: National Natural Science Foundation of China; contract/grant number: 50076043

Received 24 June 2002
Revised 23 December 2002

experimental data show a near-parabolic distribution [1]. Since swirl introduces intense tangential streamline curvature and hence curvature–turbulence interaction affects all six independent stress components, second-order closures have been suggested for modelling of swirling flows [2–4]. However, the extra computational cost and the careful numerical method prevent them from being widely applied. Non-linear eddy-viscosity turbulence models offer a better balance between accuracy and cost [1, 5]. The quadratic terms and the strain/vorticity-dependent coefficients are responsible for the ability to capture anisotropy, and the cubic terms can reflect the effect of curvature [6]. The cubic term can also capture the swirling effect [7].

The present study aims at investigating the capability of variants of cubic eddy viscosity turbulence models on strongly swirling flows. Two experimental test cases have been selected for model validation. The first test case is an axially rotating pipe flow of Imao *et al.* [8]. The second test case is a strongly swirling confined jet flow examined by So *et al.* [9]. Four cubic eddy viscosity turbulence models under low-*Re* k–ε framework are Craft *et al.* [10] (CLS), Apsley and Leschziner [11] (AL), Shih *et al.* [1] (SHIH), Merci *et al.* [12] (MDVD). For comparison, low-*Re* k–ε model of Launder and Sharma [13] is chosen as the standard model (SKE). All models are compared under the same numerical framework, with the same discretization scheme and iterative solver.

2. GOVERNING EQUATIONS

For an isothermal, incompressible, axisymmetric swirling flow in cylindrical co-ordinates, the general form of the governing equations, including the Reynolds-averaged Navier–Stokes equations and the turbulent transport equations, can be expressed as

$$\frac{\partial(\rho\phi)}{\partial t} + \frac{\partial}{\partial x}(\rho U\phi) + \frac{1}{r}\frac{\partial}{\partial r}(r\rho V\phi) - \frac{\partial}{\partial x}\left(\Gamma_\phi \frac{\partial\phi}{\partial x}\right) - \frac{1}{r}\frac{\partial}{\partial r}\left(r\Gamma_\phi \frac{\partial\phi}{\partial r}\right) = S_\phi \tag{1}$$

where t is time. x, r, θ are the axial, radial and tangential co-ordinates, respectively, and U, V, W are the corresponding mean velocity components. ρ is the fluid density. S_ϕ is the source term and Γ_ϕ is the effective viscosity for the different variables ϕ, as given in Table I.

In Table I, $\bar{p} = p + \frac{2}{3}\rho k$, and the eddy viscosity $\mu_t = \rho C_\mu f_\mu k^2/\varepsilon$. The term D is non-zero only for models adopting homogeneous dissipation rate $\tilde{\varepsilon} = \varepsilon - D$. S_ε is designed to provide the correct near-wall viscous sublayer behaviour. f_1, f_2 and f_μ are wall damping functions. τ_{ij} is the non-linear part of the Reynolds stresses. G_k is the production rate of the turbulent kinetic energy.

3. CUBIC EDDY–VISCOSITY MODELS

The dimensionless Reynolds-stress anisotropy tensor is defined by

$$a_{ij} = \frac{\overline{u_i u_j}}{k} - \frac{2}{3}\delta_{ij} \tag{2}$$

Although the foundation and derivation of different models can differ greatly, for non-linear eddy-viscosity models up to cubic order, the stress–strain relationship in incompressible flow

Table I. The effective viscosity and the source term expressions for the independent variables in Equation (1).

Variable	ϕ	Γ_ϕ	S_ϕ
Mass	1	0	0
Axial momentum (x-direction)	U	$\mu_l + \mu_t$	$-\frac{\partial \bar{p}}{\partial x} + \frac{\partial}{\partial x}\left(\Gamma_\phi \frac{\partial U}{\partial x}\right) + \frac{1}{r}\frac{\partial}{\partial r}\left(r\Gamma_\phi \frac{\partial V}{\partial x}\right) + \frac{\partial \tau_{xx}}{\partial x} + \frac{1}{r}\frac{\partial (r\tau_{xr})}{\partial r}$
Radial momentum (r-direction)	V	$\mu_l + \mu_t$	$-\frac{\partial \bar{p}}{\partial r} + \frac{\partial}{\partial x}\left(\Gamma_\phi \frac{\partial U}{\partial r}\right) + \frac{1}{r}\frac{\partial}{\partial r}\left(r\Gamma_\phi \frac{\partial V}{\partial r}\right) - \frac{2\Gamma_\phi V}{r^2} + \frac{\rho W^2}{r} + \frac{\partial \tau_{rx}}{\partial x} + \frac{1}{r}\frac{\partial (r\tau_{rr})}{\partial r} - \frac{\tau_{\theta\theta}}{r}$
Tangential momentum (θ-direction)	W	$\mu_l + \mu_t$	$-\frac{\rho VW}{r} - \frac{W}{r^2}\frac{\partial}{\partial r}(r\Gamma_\phi) + \frac{\partial \tau_{\theta x}}{\partial x} + \frac{1}{r^2}\frac{\partial (r^2\tau_{\theta r})}{\partial r}$
Turbulent kinetic energy	k	$\mu_l + \mu_t/\sigma_k$	$G_k - \rho\varepsilon - \rho D$
Dissipation rate	ε	$\mu_l + \mu_t/\sigma_\varepsilon$	$\frac{\varepsilon}{k}(C_l f_1 G_k - C_2 f_2 \rho\varepsilon) + \rho S_\varepsilon$

may be written in the following canonical form

$$a_{ij} = -2C_\mu f_\mu s_{ij} + A_{ij} \tag{3}$$

$$\begin{aligned} A_{ij} = {} & \beta_1(s_{ik}s_{kj} - \tfrac{1}{3}s_{kl}s_{kl}\delta_{ij}) + \beta_2(w_{ik}s_{kj} - s_{ik}w_{kj}) + \beta_3(w_{ik}w_{kj} + \tfrac{1}{3}w_{kl}w_{kl}\delta_{ij}) \\ & - \gamma_1 s_{kl}s_{kl}s_{ij} + \gamma_2 w_{kl}w_{kl}s_{ij} - \gamma_3(w_{ik}w_{kl}s_{lj} + s_{ik}w_{kl}w_{lj} + w_{kl}w_{kl}s_{ij} - \tfrac{2}{3}w_{kl}s_{lm}w_{mk}\delta_{ij}) \\ & - \gamma_4(w_{ik}s_{kl}s_{lj} - s_{ik}s_{kl}w_{lj}) \end{aligned} \tag{4}$$

The non-linear part of the Reynolds stresses

$$\tau_{ij} = -\rho k A_{ij} \tag{5}$$

Under the k–ε framework, the components of dimensionless mean strain and mean vorticity tensors are denoted by

$$\begin{aligned} & s_{11} = \frac{k}{\varepsilon}\frac{\partial U}{\partial x}, \quad s_{12} = \frac{k}{2\varepsilon}\left(\frac{\partial U}{\partial r} + \frac{\partial V}{\partial x}\right), \quad s_{13} = \frac{k}{2\varepsilon}\frac{\partial W}{\partial x} \\ & s_{22} = \frac{k}{\varepsilon}\frac{\partial V}{\partial r}, \quad s_{23} = \frac{k}{2\varepsilon}\left(\frac{\partial W}{\partial r} - \frac{W}{r}\right), \quad s_{33} = \frac{k}{\varepsilon}\frac{V}{r} \\ & w_{12} = \frac{k}{2\varepsilon}\left(\frac{\partial U}{\partial r} - \frac{\partial V}{\partial x}\right), \quad w_{13} = -\frac{k}{2\varepsilon}\frac{\partial W}{\partial x}, \quad w_{23} = -\frac{k}{2\varepsilon}\left(\frac{\partial W}{\partial r} + \frac{W}{r}\right) \end{aligned} \tag{6}$$

Note that $s_{ij} = s_{ji}$ and $w_{ij} = -w_{ji}$.

3.1. *Craft, Launder & Suga (1996) [10] (CLS)*

Coefficients of this model are optimized over a wide range of flows:

$$C_\mu = \frac{0.3\{1 - \exp[-0.36/\exp(-0.75\eta)]\}}{1 + 0.35\eta^{3/2}}, \quad \eta = \max(\bar{s}, \bar{w}) \tag{7}$$

where the dimensionless strain invariant and vorticity invariant can be written as

$$\bar{s} \equiv \sqrt{2s_{kl}s_{kl}}, \quad \bar{w} \equiv \sqrt{2w_{kl}w_{kl}} \tag{8}$$

$$\beta_1 = 0.4C_\mu f_\mu, \quad \beta_2 = 0.4C_\mu f_\mu, \quad \beta_3 = -1.04C_\mu f_\mu$$

$$\gamma_1 = \gamma_2 = 40C_\mu^3 f_\mu, \quad \gamma_3 = 0, \quad \gamma_4 = -80C_\mu^3 f_\mu \tag{9}$$

$$f_\mu = 1 - \exp[-\sqrt{R_t/90} - (R_t/400)^2] \tag{10}$$

$$f_1 = 1, \quad f_2 = 1 - 0.3\ \exp(-R_t^2) \tag{11}$$

where $R_t \equiv k^2/v\varepsilon$ is the turbulent Reynolds number.

$$D = 2v\left(\frac{\partial\sqrt{k}}{\partial x_i}\right)^2 \tag{12}$$

When $R_t \leqslant 250$, $S_\varepsilon = 0.0022\ \frac{\bar{s}v_t k^2}{\varepsilon}(\frac{\partial^2 U_i}{\partial x_j \partial x_k})^2$; otherwise, $S_\varepsilon = 0$.

3.2. *Apsley and Leschziner (1998) [1] (AL)*

The stress–strain relationship is formed by successive iterative approximations to an algebraic Reynolds-stress model. Free coefficients are calibrated by reference to DNS data for a channel flow.

$$C_\mu = \frac{-a_{12}^* f_P}{(1 + \bar{\beta}^2/3 - \bar{\gamma}^2)\sigma^*} \tag{13}$$

$$\beta_1 = 6(a_{11}^* - a_{22}^*)(f_P/\sigma^*)^2, \quad \beta_2 = (a_{11}^* - a_{22}^*)(f_P/\sigma^*)^2, \quad \beta_3 = 0$$

$$\gamma_1 = \tfrac{4}{3}C_\mu\bar{\beta}^2(f_P/\sigma^*)^2, \quad \gamma_2 = 4C_\mu\bar{\gamma}^2(f_P/\sigma^*)^2$$

$$\gamma_3 = 6C_\mu\bar{\gamma}^2(f_P/\sigma^*)^2, \quad \gamma_4 = 6C_\mu\bar{\beta}\bar{\gamma}(f_P/\sigma^*)^2 \tag{14}$$

$$f_\mu = f_1 = f_2 = 1, \quad D = 0 \tag{15}$$

$$S_\varepsilon = C_2 f_2 \frac{\varepsilon^{(1)}\varepsilon}{k}\ \exp(-0.0038y^{*2}), \quad \varepsilon^{(1)} = \frac{C_\mu^{*3/4}k^{3/2}}{l_\varepsilon^{(1)}}, \quad C_\mu^* = 0.09 \tag{16}$$

$$\bar{\beta} = 0.222, \quad \bar{\gamma} = 0.623 \tag{17}$$

The dissipation length is based on the results of DNS data:

$$l_\varepsilon^{(1)} = 0.179\,y_n(1 + 128/y^*)[1 - \exp(-y^{*2}/279)] \tag{18}$$

where y_n is the distance from the nearest wall and $y^* \equiv y_n\sqrt{k}/v$ is a dimensionless distance.

The anisotropy-tensor components a_{ij}^* and the shear parameter σ^* in equilibrium condition are calibrated from DNS data for plane channel flow:

$$
\begin{aligned}
a_{11}^* &= 1 + 0.42\ \exp(0.296\sqrt{y^*} - 0.040y^*) - 2/3 \\
a_{22}^* &= 0.404[1 - \exp(0.001y^* - 0.000147y^{*2})] - 2/3 \\
a_{12}^* &= -0.3[1 - \exp(-0.00443\sqrt{y^*} - 0.0189y^*)] \\
\sigma^* &= 3.33[1 - \exp(-0.45y^*)][1 + 0.277y^{*3/2}\ \exp(-0.088y^*)]
\end{aligned} \tag{19}
$$

The constants in turbulent transport equations are

$$
c_1 = 1.44, \quad c_2 = 1.83, \quad \sigma_k = \frac{1.0}{1 + \bar{\beta}^2/3 - \bar{\gamma}^2}, \quad \sigma_\varepsilon = \frac{1.37}{1 + \bar{\beta}^2/3 - \bar{\gamma}^2} \tag{20}
$$

The non-equilibrium parameter which accounts for departures of the local shear parameter $\sigma = \sqrt{s_{kl}s_{kl} + w_{kl}w_{kl}}$ is

$$
\begin{aligned}
f_P &= \frac{2f_0}{1 + \sqrt{1 + 4f_0(f_0 - 1)(\sigma/\sigma^*)^2}} \\
f_0 &= 1 + 1.25\ \max(0.09\sigma^{*2}, 1.0)
\end{aligned} \tag{21}
$$

3.3. *Shih et al. (1997) [1] (SHIH)*

The cubic constitutive relation for the Reynolds stresses is derived using the invariant theory in continuum mechanics and the generalized Cayley–Hamilton formulations.

The stress–strain relationship for incompressible flow is

$$
\begin{aligned}
a_{ij} = {} & -2C_\mu f_\mu s_{ij} - A_3(s_{ik}w_{kj} - w_{ik}s_{kj}) \\
& + 2A_5(w_{ik}s_{kl}s_{lj} - s_{ik}s_{kl}w_{lj} + w_{ik}s_{kl}w_{lj} - \tfrac{1}{3}w_{kl}s_{lm}w_{mk}\delta_{ij} + II_s s_{ij})
\end{aligned} \tag{22}
$$

where the second principal invariant of s_{ij} is $II_s = \frac{1}{2}(s_{kk}s_{mm} - s_{kl}s_{kl})$.

$$
C_\mu = \frac{1}{4.0 + A_s U^*}, \quad A_3 = \frac{\sqrt{1 - (A_s C_\mu s^*)^2}}{0.5 + 1.5w^*s^*}, \quad A_5 = \frac{6.4C_\mu f_\mu}{7(s^*)^2 + (w^*)^2} \tag{23}
$$

$$
A_s = \sqrt{6}\ \cos\ \phi, \quad \phi = \frac{1}{3}\ \arccos\left(\sqrt{6}\ \frac{s_{kl}s_{lm}s_{mk}}{(s^*)^3}\right) \tag{24}
$$

$$
s^* = \sqrt{s_{kl}s_{kl}}, \quad w^* = \sqrt{w_{ij}w_{ij}}, \quad U^* = \sqrt{s_{kl}s_{kl} + w_{kl}w_{kl}} \tag{25}
$$

$$
f_1 = 1, \quad f_2 = 1 - 0.22\ \exp(-R_t^2/36), \quad f_\mu = [1 - \exp(-a_1 y^* - a_3 y^{*3} - a_5 y^{*5})]^{1/2} \tag{26}
$$

where $a_1 = 1.7 \times 10^{-3}$, $a_3 = 1.0 \times 10^{-9}$, $a_5 = 5.0 \times 10^{-10}$.

$$D = 0, \quad S_\varepsilon = \nu\nu_t \left(\frac{\partial^2 U_i}{\partial x_j \partial x_k} \right)^2 \tag{27}$$

Wall boundary conditions for k and ε are: $k_w = 0.25u_\tau^2$, $\varepsilon_w = 0.251u_\tau^4/\nu$, where $u_\tau \equiv \sqrt{\tau_w/\rho}$ is the friction velocity and τ_w is the dynamic wall shear stress.

3.4. *Merci et al.* (*2001*) [12] (*MDVD*)

This cubic model combined with a new transport equation for the dissipation rate, in which a low-Reynolds source term is introduced. The model has been checked on different realizability constraints.

$$\mu_t = \rho C_\mu f_\mu k \tau_t, \quad C_\mu = (A_1 + A_s \max(\bar{s}, \bar{w}))^{-1} \tag{28}$$

where $\tau_t = k/\varepsilon + \sqrt{\mu/\rho\varepsilon}$ is the turbulence time scale.

$$A_1 = 8, \quad A_s = \sqrt{3} \cos \phi, \quad \phi = \tfrac{1}{3} \arccos(\sqrt{6}W), \quad W = 2^{1.5} \frac{s_{ij}s_{jk}s_{ki}}{\bar{s}^3} \tag{29}$$

$$\beta_1 = q_1, \quad \beta_2 = q_2 + q_1/6, \quad \beta_3 = 0, \quad \gamma_1 = \gamma_2 = -c, \quad \gamma_3 = 0, \quad \gamma_4 = 2c \tag{30}$$

$$q_1 = (7 + 3 \max(\bar{s}, \bar{w}) + 1.2 \times 10^{-2} \max(\bar{s}^3, \bar{w}^3))^{-1}$$

$$q_2 = (1.7 + 5.4 \max(\bar{s}, \bar{w}) + 3 \times 10^{-2} \max(\bar{s}^3, \bar{w}^3))^{-1}$$

$$\bar{s} \geqslant \bar{w}, \quad c = -600C_\mu^4; \quad \bar{s} < \bar{w}, \quad c = -\min(600C_\mu^4; 4f_\mu C_\mu/(\bar{w}^2 - \bar{s}^2)) \tag{31}$$

$$f_\mu = 1 - \exp(-4.2 \times 10^{-2}\sqrt{y^*} - 5.1 \times 10^{-4} y^{*1.5} - 3.65 \times 10^{-10} y^{*5})$$

$$f_1 = 1, \quad f_2 = 1 - 0.22 \exp\left(-\frac{Re_T^2}{36}\right) \tag{32}$$

where $Re_T = \rho k \tau_t/\mu$ is the turbulence Reynolds number.

$$D = 0, \quad S_\varepsilon = 0 \tag{33}$$

In the transport equation for ε, $C_2 = 1.83 + 0.075\bar{w}/(1 + \bar{s}^2)$, which depends on the rotation. The source term of the dissipation rate equation is

$$(C_1 f_1 G_k - C_2 f_2 \rho\varepsilon)/\tau_t + E \tag{34}$$

where $E = -1.8(1 - f_\mu)(\mu + \mu_t/\sigma_\varepsilon)(\partial k/\partial x_i)\partial\tau_t^{-1}/\partial x_i$ is the cross-diffusion term, which only has an influence near the wall.

4. NUMERICAL METHOD

All models are computed by the same code based on the finite-volume method with non-orthogonal grids [14]. Variable storage is co-located and cell-centred, with Rhie–Chow interpolation for cell-face mass fluxes. The SIMPLE pressure–correction algorithm is used to

obtain the pressure field. The convection and diffusion terms of all the equations, including the momentum equations in three directions and the model transport equations for turbulence quantities, are approximated by the second-order central differencing scheme. The deferred correction technique has been used for the discretization of the convection term. The Stone's strongly implicit procedure (SIP) method is employed with under-relaxation factors.

Convergence is judged by monitoring the magnitude of the absolute residual sources of mass and momentum, normalized by the respective inlet fluxes. The iteration is continued until all above residuals fell below 0.05%.

5. RESULTS AND DISCUSSIONS

5.1. Axially rotating pipe flow

Imao *et al.* [8] conducted this experiment to study the effects of the swirl driven by a rotating pipe wall on turbulent flow characteristics. The pipe inner diameter D is 30 mm. According to the experiment, a fully developed flow was established after the pipe length $L = 120D$. The dimensionless rotation rate $N = 0.5$, where

$$N = W_{\text{wall}}/u_{\text{m}} \tag{35}$$

In the above definition, W_{wall} is the tangential wall velocity and u_{m} is the bulk mean axial velocity. The Reynolds number based on u_{m} and D is 20 000.

At the entrance, uniform axial velocity was specified. With the pipe rotation, the flow developed axially, radially and tangentially. A 200×120 highly stretched non-uniform grid was used, ensuring $y^+ < 0.5$ along the first grid-line from the wall.

The final developed axial and tangential velocity profiles are shown in Figure 1. SKE is completely unable to capture any swirl effect. The results show that SKE yields a solid body rotation, while all cubic models correctly represent the parabolic distribution of tangential velocity. Also axial velocity profile is described well by cubic models.

A fully developed rotating pipe flow provides a very clear test case for checking the turbulence model's ability to model swirling flows [1]. In cubic models except for AL, the coefficients of cubic terms γ_3 and γ_4 are calibrated by studying this flow, which results in $\gamma_3 = 0$. However, it is shown that both γ_3 and γ_4 cubic terms are important [7]. Therefore, there exist some restrictions in these models.

5.2. Jet in strongly swirling confined flow

Experimental data had been obtained by So *et al.* [9]. This case is designed to examine the interaction between swirl-induced curvature and turbulence. The flow geometry is shown in Figure 2. A strongly swirling outer flow, characterized by the swirl number

$$S = \int_0^R UWr^2 \, \mathrm{d}r \Big/ R \int_0^R U^2 r \, \mathrm{d}r = 2.25 \tag{36}$$

was introduced into a chamber of radius $R = 62.5$ mm together with a central non-swirling jet of diameter $d = 8.73$ mm. The latter is introduced to inhibit extensive reverse flow along the centreline. The average velocity upstream was about 6.8 m/s. Based on it and the diameter of

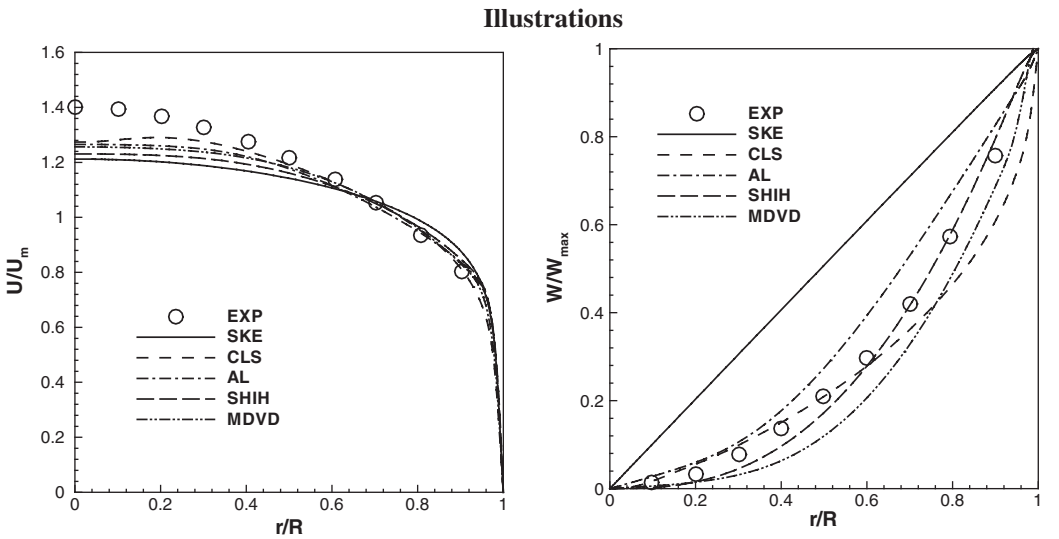

Figure 1. Fully developed axial and tangential velocity profiles in the axially rotating pipe.

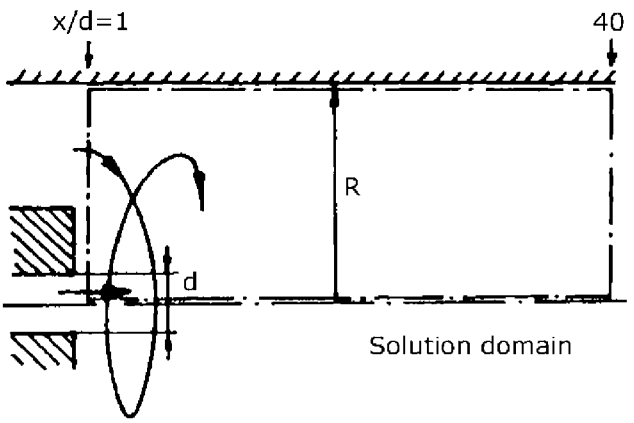

Figure 2. Geometry of strongly swirling-confined jet flow.

the test section, the characteristic Reynolds number was $Re = 5.49 \times 10^4$. The axial velocity at the jet exit is 25.4 m/s, which makes the jet Reynolds number $Re_j = 1.438 \times 10^4$ based on d.

The inlet plane was located at $x/d = 1$, where the measured data were specified. The turbulent kinetic energy k is calculated from the measured and assumed normal stresses. The dissipation rate is calculated as $\varepsilon = k^{1.5}/0.36R$ [2]. Because of the strongly swirling condition, the flow is close to subcritical. It was found that subcritical state flow is highly sensitive to the perturbation far downstream [15]. Therefore, at the exit plane $x/d = 40$, the measured axial velocity is prescribed to avoid the predictive uncertainties [2]. Zero-gradient conditions are adopted for all other variables. At both inlet and exit planes, the measured axial velocity

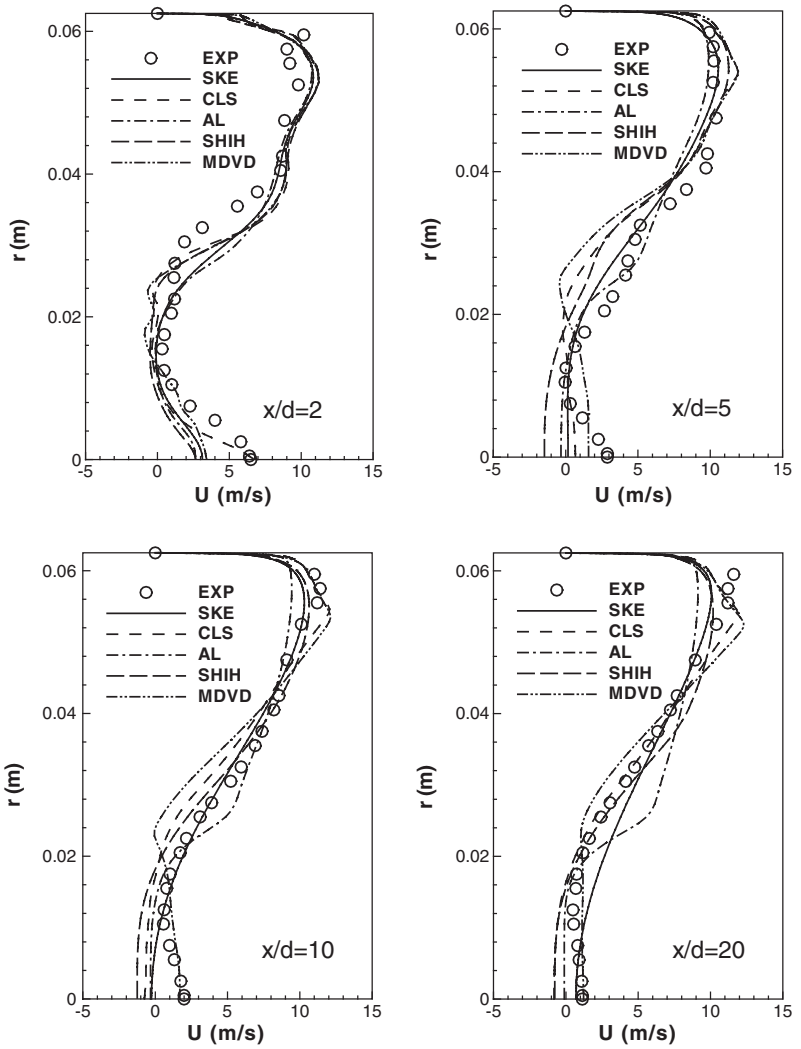

Figure 3. Axial velocity profiles.

profiles have been corrected slightly by about 6% in total so that they both correspond to the measured mass flow rate of 104.8 gm/s.

The grid with 150×50 cells is employed, which is fine enough to minimize the effects of numerical diffusion [16]. This non-uniform grid ensures $y^+ < 0.2$ along the first grid-line from the wall for the use of low-Reynolds-number turbulence models.

Figure 3 present the axial velocity profiles at different locations. SHIH predicts a rapid decay of centreline velocity and gives a large reserve flow region along the centreline. This perhaps suggests an overestimation of swirl-induced turbulence damping. It is clear to see that MDVD simulates the decay of central jet correctly.

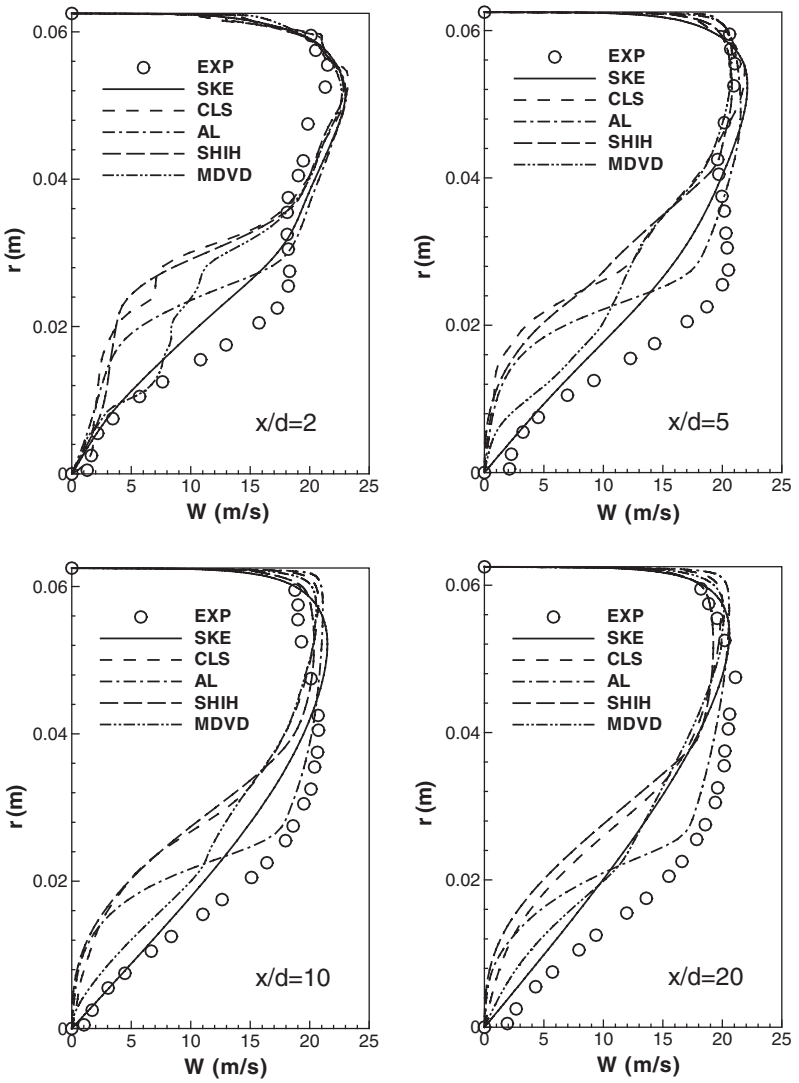

Figure 4. Tangential velocity profiles.

Figure 4 show the tangential velocity profiles. SKE predicts a solid body profile of the tangential velocity, while cubic models mimic the observed combined forced-free vortex motion. The result of AL agrees with experimental data fairly well. This is due to the special consideration of model derivation and calibration. The stress–strain relationship of AL is formed by successive iterative approximations to an algebraic stress model (ASM), and the free coefficients are just calibrated by DNS data of a channel flow so that the special calibration of cubic term is avoided.

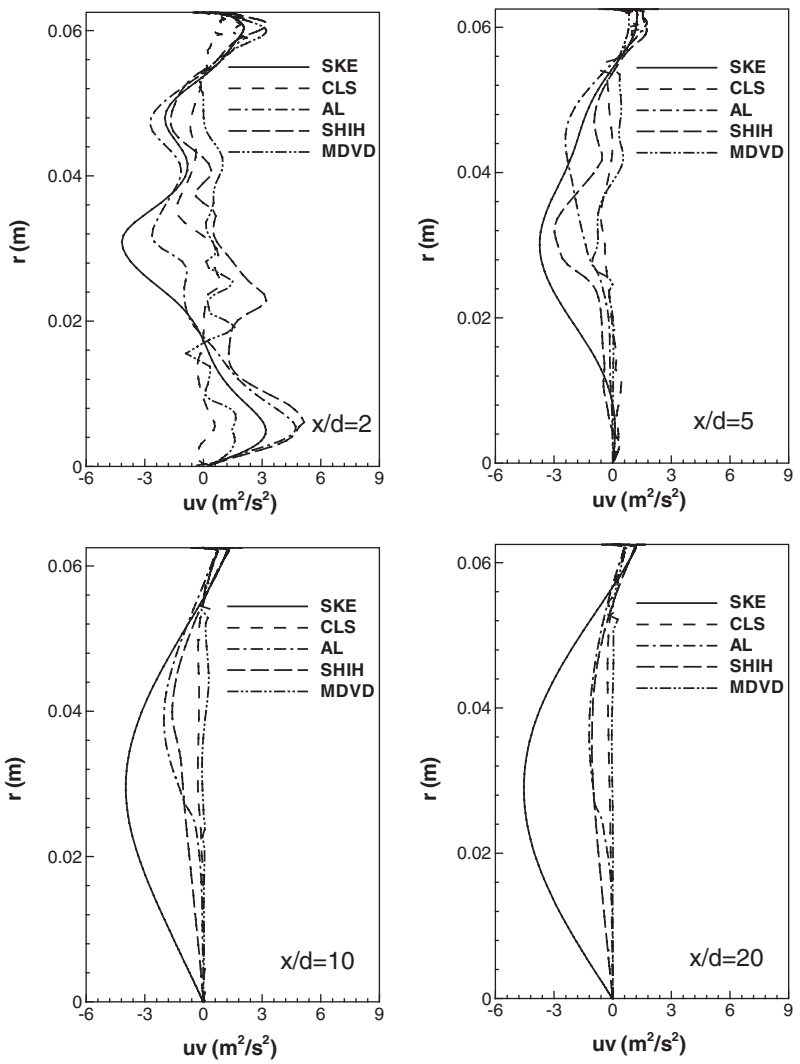

Figure 5. Shear stress $\overline{uv}$ profiles.

In Figure 5, the cubic model predictions indicate a lower level of shear stress $\overline{uv}$, whereas no measured data are available to support the simulation. The reduction of the shear stress level produced by cubic models is responded to swirl-induced strains.

The predicted turbulence intensities are compared with the experiment in Figures 6 and 7. Both the measurements and predictions show nearly isotropic normal stresses. None of the models satisfactorily predicts the turbulence intensities. The cubic models return a lower level of normal stresses in response to the swirl-related strain at this high level of swirling flow and agree with the measurements. A subcritical state appears to reflect a strong decay in turbulent

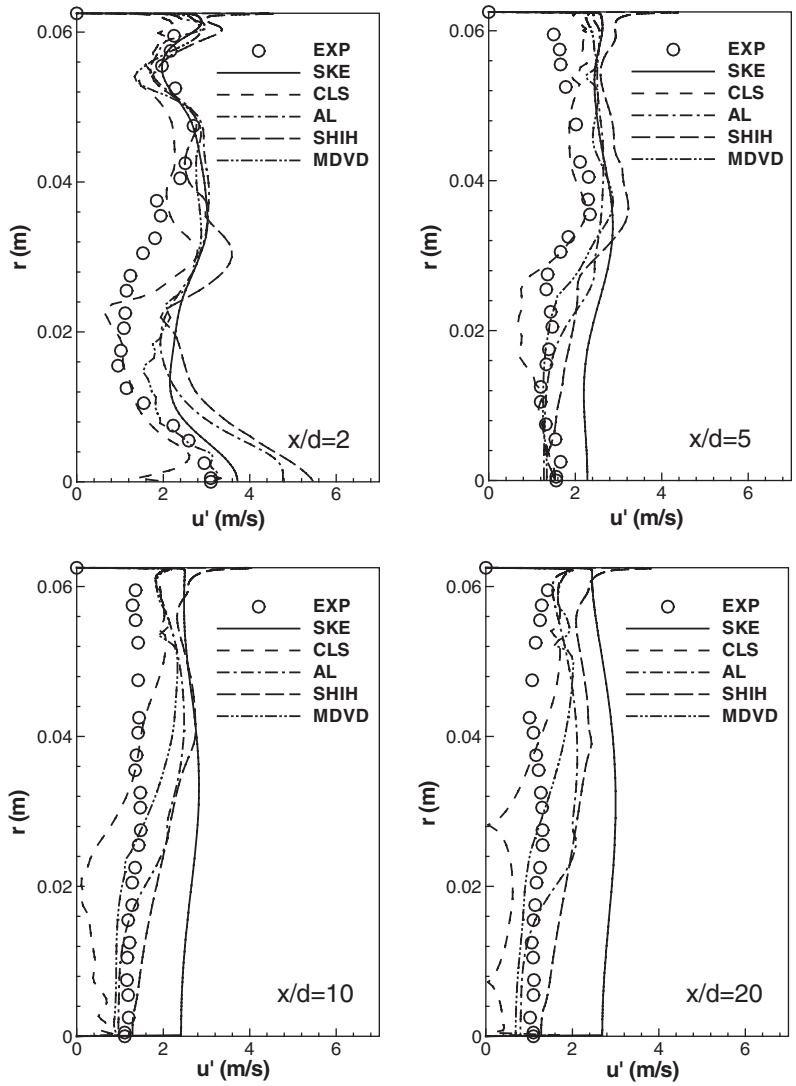

Figure 6. Axial turbulence intensity profiles.

mixing. SKE fails to capture the subcritical nature of the flow, whereas cubic models appear to represent the primary flow features correctly.

It is interesting to compare the performances of MDVD and MDVD2 (MDVD without the γ_4 term). Figures 8 and 9 show the results of axial and tangential velocity profiles by these two models, respectively. It can be seen that MDVD2 obtains results closer to the measurements. This is difficult to explain. However, a fully developed rotating pipe flow provides a too simple test case for determining the cubic terms, so a more precise calibration is necessary.

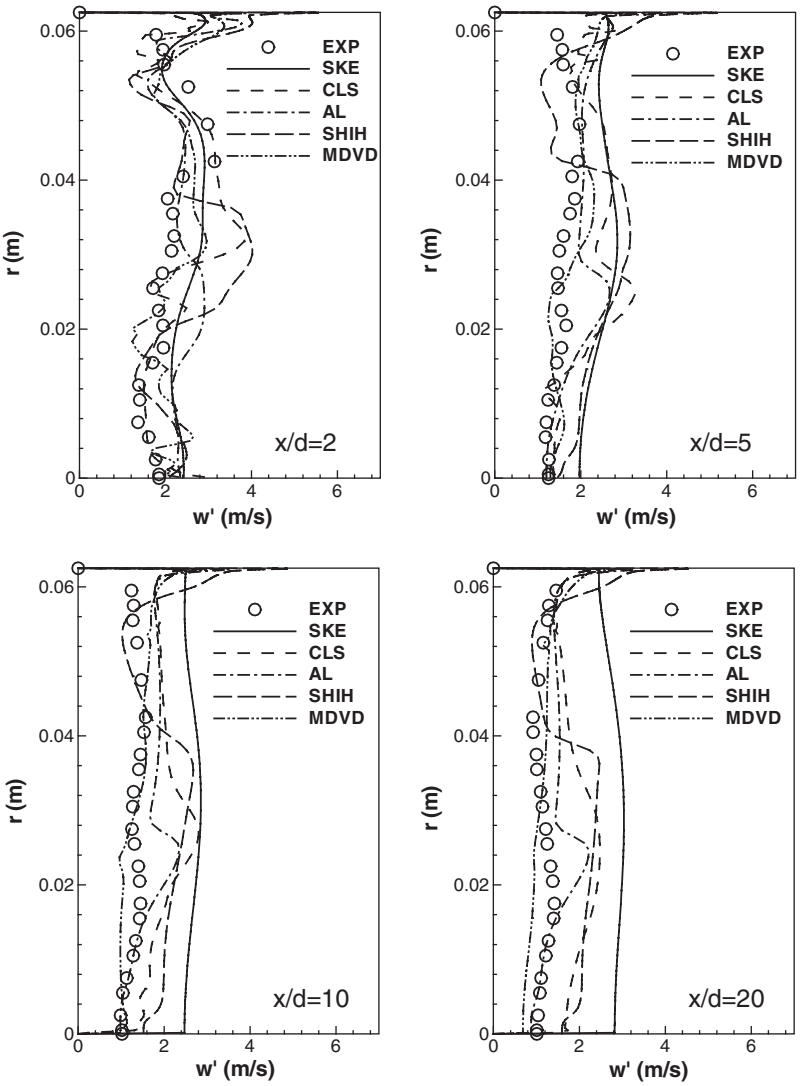

Figure 7. Tangential turbulence intensity profiles.

6. CONCLUSIONS

The present studies demonstrate the superiority of cubic models over SKE in the prediction of strongly swirling flows. SKE does not contain any mechanism to describe the stabilizing effects of swirling motion and as a consequence it performs poorly. While cubic models are sensitive to the swirl-induced body forces and reproduce the major features of the subcritical flow, including the strong stabilizing effects of the swirl on the Reynolds stresses and tangential velocity, which are in reasonable agreement with the measurements.

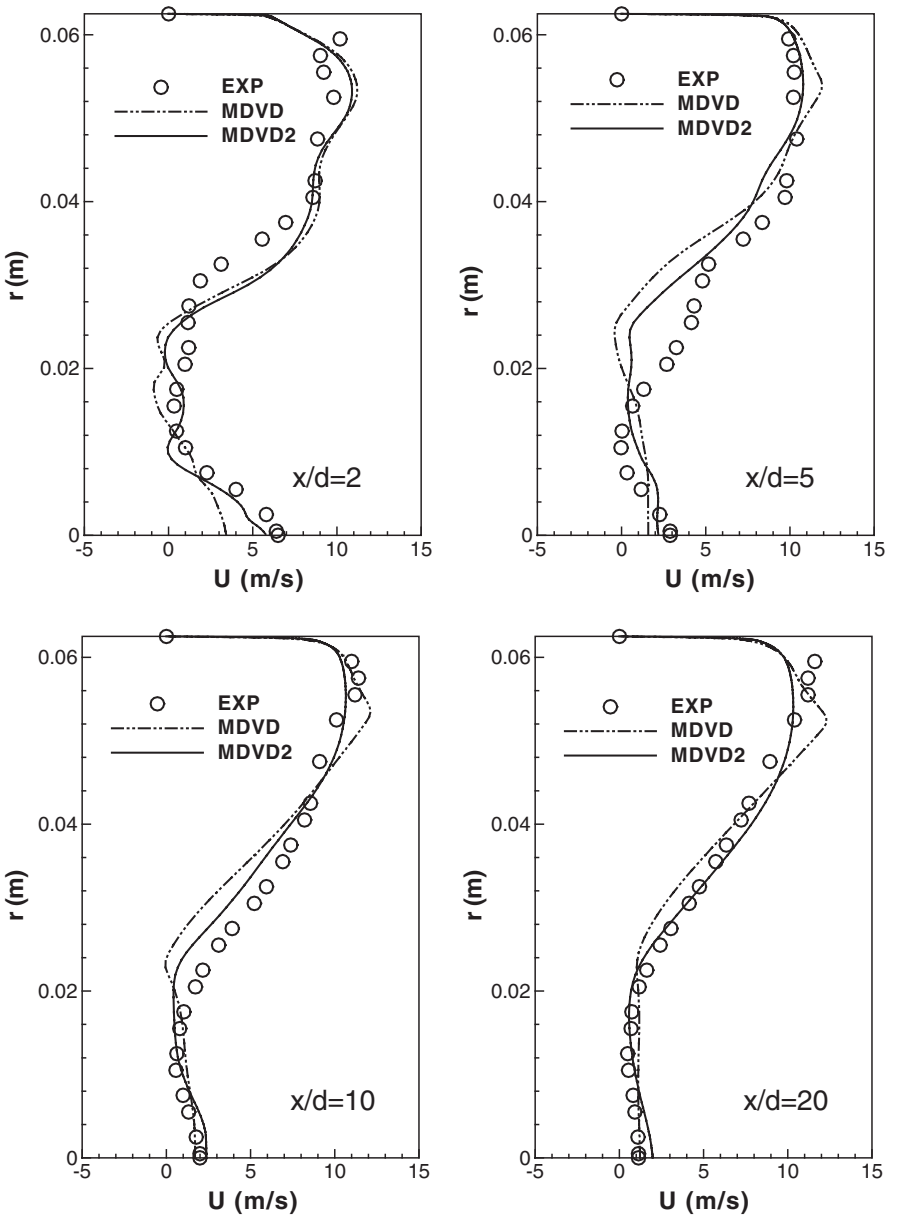

Figure 8. Axial velocity profiles of MDVD.

A fully developed rotating pipe flow does not contain enough flow physics, hence is too simple for calibrating the cubic-order turbulence model and the calibration of cubic terms is still a topic of investigation. The results of AL show that explicit algebraic stress models (EASM) provide an effective approach to predict strongly swirling flows, which require fewer calibrations and contain more flow physics.

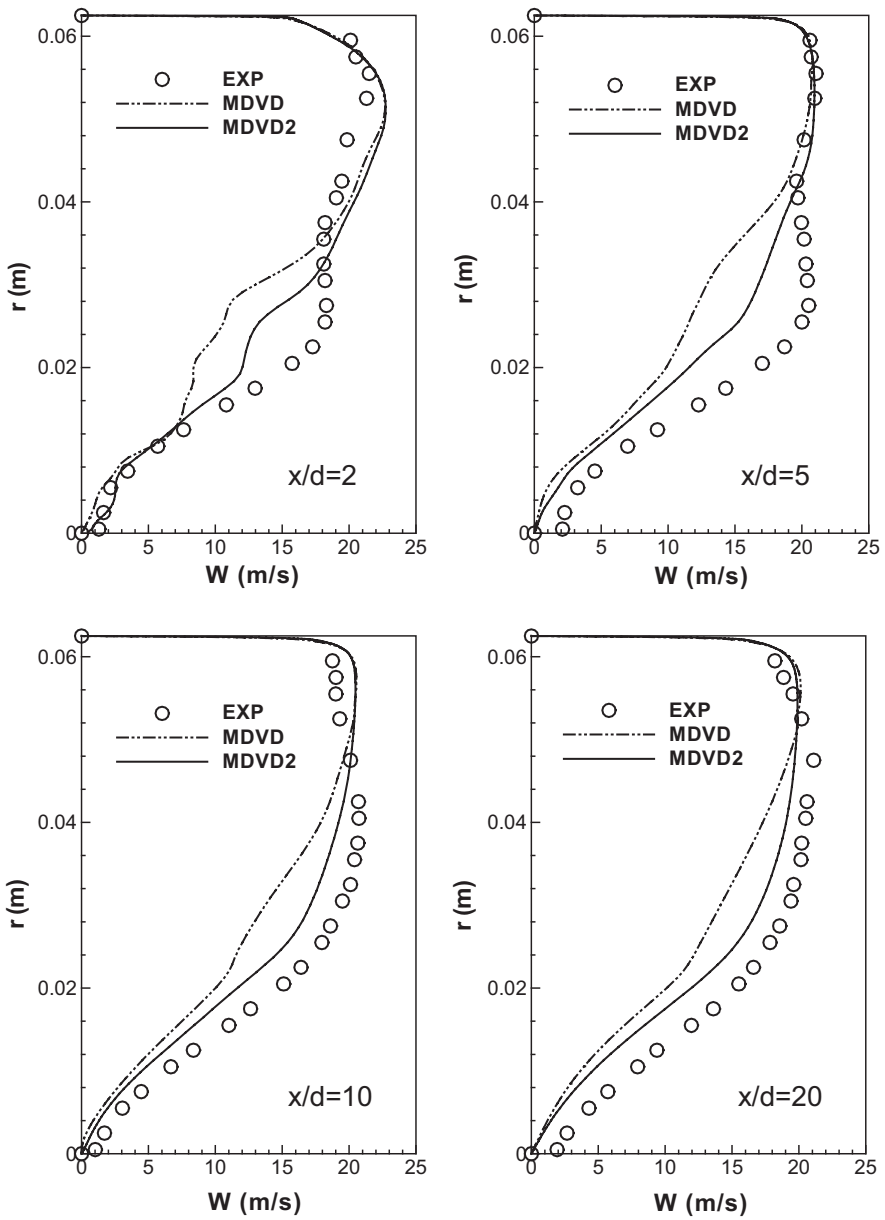

Figure 9. Tangential velocity profiles of MDVD.

ACKNOWLEDGEMENTS

The financial support provided by the National Natural Science Foundation of China (50076043) is gratefully acknowledged.

REFERENCES

1. Shih T-H, Zhu J, Liou WW, Chen K-H, Liu J-S, Lumley J. Modelling of turbulent swirling flows. *NASA TM* 113112, 1997.
2. Hogg S, Leschziner MA. Computation of highly swirling confined flow with a Reynolds stress turbulence model. *AIAA Journal* 1989; **27**:57–63.
3. Jones WP, Pascau A. Calculation of confined swirling flows with a second moment closure. *Journal of Fluids Engineering* 1989; **111**:248–254.
4. Chen JC, Lin CA. Modelling strongly swirling flows with second moment closure. *International Journal for Numerical Methods in Fluids* 1999; **30**:493–508.
5. Nikjoo M, Mongia HC. Study of nonlinear k–ε model for turbulent swirling flows. *AIAA Paper* 98-3984, 1998.
6. Leschziner MA. Turbulence modelling for separated flows with anisotropy-resolving closures. *Philosophical Transactions of the Royal Society of London A* 2000; **358**:3247–3277.
7. Speziale CG, Younis BA, Berger SA. Analysis and modelling of turbulent flow in an axially rotating pipe. *Journal of Fluid Mechanics* 2000; **407**:1–26.
8. Imao S, Itoh M, Harada T. Turbulent characteristics of the flow in an axially rotating pipe. *International Journal of Heat and Fluid Flow* 1996; **17**:444–451.
9. So RMC, Ahmed SA, Mongia HC. An experimental investigation of gas jets in confined swirling air flow. *NASA CR* 3832, 1984.
10. Craft TJ, Launder BE, Suga K. Development and application of a cubic eddy-viscosity model of turbulence. *International Journal of Heat and Fluid Flow* 1996; **17**:108–115.
11. Apsley DD, Leschziner MA. A new low-Re non-linear two-equation turbulence model for complex flows. *International Journal of Heat and Fluid Flow* 1998; **19**:209–222.
12. Merci B, De Langhe C, Vierendeels J, Dick E. A quasi-realizable cubic low-Reynolds eddy-viscosity turbulence model with a new dissipation rate equation. *Flow*, *Turbulence and Combustion* 2001; **66**:133–157.
13. Launder BE, Sharma BI. Application of the energy-dissipation model of turbulence to the calculation of flow near spinning disc. *Letters of Heat and Mass Transfer* 1974; **1**:131–138.
14. Ferziger JH, Perić M. *Computational Methods for Fluid Dynamics*. Springer: Berlin, 1996.
15. Escudier MP, Keller JJ. Recirculation in swirling flow: a manifestation of vortex breakdown. *AIAA Journal* 1985; **23**:111–116.
16. Durst F, Wennerberg D. Numerical aspects of calculation of confined swirling flows with internal recirculation. *International Journal for Numerical Methods in Fluids* 1991; **12**:203–224.

